Observations of Surface Wave Dispersion in the Marginal Ice Zone

Clarence Collins[1], Martin Doble[2], Björn Lund[3], and Madison Smith[4]

[1]Coastal and Hydraulics Laboratory, U.S. Army Engineering Research and Development Center, Duck, NC
[2]Polar Scientific Ltd, UK
[3]Department of Ocean Sciences, University of Miami, Miami, FL
[4]Applied Physics Laboratory, University of Washington, Seattle, WA

Key Points:

- Marine radar and surface buoys are utilized to estimate wavenumber in sea ice
- Wave dispersion did not deviate from the linear dispersion relation for frequencies 0.10 - 0.30 Hz
- A small increase in wavenumber was observed 0.30 - 0.50 Hz, consistent with mass loading

Corresponding author: Clarence Collins, `Clarence.O.Collins@usace.army.mil`

Abstract

To date, this study presents the most comprehensive set of *in situ* and remote measurements of wavenumber, and hence the dispersion relation, in ice. A number of surface following buoys were deployed from the R/V Sikuliaq, which also hosted an X-band marine radar, in icy conditions during the ONR Arctic Sea State field experiment. The heave-slope correlation method was used to estimate the root-mean-square wavenumber from the buoys. The method was highly sensitive to noise, and extensive quality control measures were developed to isolate real signals in the estimated wavenumber. The buoy measurements were complemented by shipboard marine X-band radar dispersion measurements, which are limited to lower frequencies (< 0.32 Hz). Overall, deviation from the open water linear dispersion relation was not significant, and matched the open water relation nearly exactly for the range 0.10 - 0.30 Hz. Isolating a subset of data during the strongest wave event showed evidence of increased wavenumbers at frequencies greater than 0.30 Hz. The ice conditions and deviation from linear dispersion were qualitatively consistent with mass loading. The dispersion curves did not exactly fit a mass loading model, suggesting either measurement error or other processes at play.

1 Introduction

Accurate prediction of surface wave properties on oceans and lakes in the presence of ice is important for safe navigation and operations. In the Arctic Ocean, changing climate has led to increasing fetch and has greatly enhanced the presence of waves [*Thomson and Rogers*, 2014]. The changing Arctic wave climate was the focus of an Office of Naval Research (ONR) Departmental Research Initiative (DRI) called "Sea State and Boundary Layer Physics in the Emerging Arctic Ocean" (often abbreviated to Arctic Sea State). A number of wave experiments were performed during the Arctic Sea State field campaign, aimed at studying various wave-ice interaction processes. Although data are used from various wave experiments, special attention is payed to the most energetic wave event during Wave Experiment 3 (WE3).

For wave prediction, the 3rd generation spectral wave model Wavewatch III [*The WAVEWATCH III ® Development Group*, 2016] has a number of source terms to represent the ice effects on waves [*Rogers and Zieger*, 2014; *Collins III and Rogers*, 2017] *Thomson et al., [this issue]*. The source terms range from highly empirical to those which are based on material physics. The physics based source terms involve solving a complex dispersion equation which accounts for the material properties of ice cover. For in-ice dispersion, there are explicit terms for additional inertia at the surface (also called "mass loading"), effective elasticity, and effective viscosity. The imaginary part of dispersion is related to the attenuation rate, and the real part to a change in wavenumber. A change in wavenumber manifests itself through the shoaling and refraction, analogous to waves approaching shallow water or gradients in surface currents. While attenuation has been well studied (e.g. *Wadhams et al.* [1988], Stopa et al., this issue), relatively little attention has been paid to the change in wavenumber outside of theoretical models. Thus, data from the Arctic Sea State field experiment represent an opportunity to address this gap in the literature.

Free of ice, the frequency-wavenumber dispersion relationship in deep water and for small amplitude waves (Airy wave theory), is as follows:

$$k_{ow} = \frac{(2\pi f)^2}{g} \tag{1}$$

Where f is the frequency, g is gravitational acceleration, and k_{ow} is wavenumber in open water [*Kinsman*, 1965]. This theoretical relationship has been verified and found to be appropriate under *most* oceanic conditions [e.g., *Longuet-Higgins*, 1963]. Small deviations from this relationship arise in very particular situations. If waves are sufficiently steep, the wave amplitude begins to affect dispersion [*Stokes*, 1847]. If waves are sufficiently short, surface tension becomes important [*Lamb*, 1932]. In a pure wind sea, far away from the peak of the wave spectrum, f_p, nonlinear contributions tend to dominate over free waves ($f < f_p$ and $f > 4f_p$) [*Krogstad*, 2002; *Leckler et al.*, 2015].

In contrast to open water conditions, little is known about how wavenumber may be changed in ice cover because *in situ* measurements are very rare (see the recent survey of wave observations in polar regions in *Collins III et al.* [2017a]). Evidence suggests that elasticity is important for solid ice sheets and pack ice [*Squire and Allan*, 1977; *Sutherland and Rabault*, 2016; *Marsan et al.*, 2012], but little is for certain in the marginal ice zone (MIZ) with loose floes of various sizes, thickness, ages, and arrangements. The Arctic Sea State wave experiments were characterized by loose pancake and frazil ice fields. Previous to this study, the only observations of wavenumber in the MIZ were those of *Fox and Haskell* [2001], we reproduce a summary from *Collins III et al.* [2017a]:

> In the Antarctic MIZ, Fox and Haskell (2001) mounted two accelerometers to two elliptic pancake ice floes. The floes were estimated to be 0.3 and 0.6 m thick, but were not otherwise characterized. By choosing two closely located positions, they were able to estimate the propagation speeds of waves (and hence indirectly the wavelength) in ice by measuring the frequency spectrum. Their Figure 6 shows that the fitted empirical wavelength is slightly longer for frequencies within the 0.05 – 0.10 Hz band and then significantly shorter for frequencies from the 0.10 – 0.16 Hz band and a fitted dispersion relation gave $k \propto \omega^{2.41}$. For comparison the open water relation gives $k \propto \omega^2$. It is difficult to explain the lengthening of the low frequencies, but the decrease in wavelength of high frequency waves is essentially consistent with mass loading.

The observations of *Fox and Haskell* [2001] are ostensibly intuitive because the size of individual ice floes was much less than characteristic wavelength. This disparity in scales ensured that 1) scattering was not dominant and 2) the elasticity of individual floes would not impact wave propagation.

The scale of wavelength and ice floes are similar in the cases presented here to those in *Fox and Haskell* [2001]. However, scales do not give the full picture as effective material properties of the ice can be important. Based on hourly visual observations, the primary ice type for the vast majority of these measurements was pancake ice, frazil ice, or small floes of thin young ice. These ice types would have been free of internal stress and for all cases ice thickness, h, was less than 1 m. For WE3 ice thickness $h \leq 0.3$ m. Although it is possible to measure the properties of individual ice floes [*Marchenko et al.*, 2011], the effective properties of a conglomerate of disparate floes can only be inferred by measuring the wave properties and inverting a viscoelastic model. Using Arctic Sea State data, *Cheng et al.* [2017] calibrated a viscoelastic dispersion model based on the idea of effective material properties and found that shear modulus and viscosity ranged over several orders of magnitude. During WE3, most values clustered around very low shear modulus (effectively 0) and a value of viscosity around 2 - 10 m^2/s (about 2 orders of magnitude what *Newyear and Martin* [1999] found for grease ice in the laboratory). The effect of the added inertia of the ice, as described by the mass loading (ML) model, is always present and dominant when viscosity and shear modulus are small. Even if the viscosities values of *Cheng et al.* [2017] are accurate, combined with the ice thickness less than 0.3 m and the range of observable frequencies, mass loading would tend to dominate the change in wavenumber in lower frequencies and the overall effect would be small (see Fig. 6 of *Collins III et al.* [2017a]). While other effects tend to decrease wavenumber, ML tends to increase the wavenumber [*Collins III et al.*, 2017a]. Like most changes to dispersion, it is preferentially strong in the high frequencies, explaining the results of *Fox and Haskell* [2001].

Thomson et al. [this issue] give a detailed exposé of the Arctic Sea State DRI. The pertinent aspects for this study include the deployment of a number of wave measuring, Lagrangian buoys referred to as the wave buoys (WB1–7) and the shipboard X-band marine radar (MR). Of these, only MR offers a spatio-temporal measurement capable of directly mapping the wave energy on a frequency-wavenumber (f, k_x, k_y) dispersion surface. Unfortunately, the observable range of waves for the MR are limited ($<$ 0.32 Hz). The WB observations can be used to estimate the root-mean-square (RMS) wavenumber nominally out to ~0.50 Hz. This is important because wave effects on ice are more prominent in the high frequencies, a fact that is well documented for attenuation (often described as the low pass filtering effect of ice) [*Collins III et al.*, 2015; *Marko*, 2003]. In the dispersion paradigm, attenuation and change in wavenumber are two sides of the same coin. Thus, deviation from linear dispersion is expected to be particularly prominent in the high frequencies. Although MR offers a more complete picture of dispersion within its observational range, the WBs were able to observe the high frequencies where deviations are more likely to appear. Therefore, the WB data are the focus of this study.

While there are a number of analytic dispersion models, the main goal of this study is to simply present observations of the deviation from linear dispersion rather than quantitatively evaluating the various dispersion models. First, we present MR results covering all major wave experiments during Arctic Sea State (Section 2.1). A slope-correlation technique is used on the WB data (section 2.2.1) which requires careful quality control (section 2.2.2) to obtain point estimates of root-mean-square (RMS) wavenumber. We isolate wave experiment 3 to analyze variations in the deviation of wavenumber in both time and space (section 2.3). Deviations from linear dispersion occur at the high frequencies and are characterized by an increase in wavenumbers (section 3). This type of behavior is congruent with ML. We furthermore discuss this result in the context of satellite based estimates of ice concentration (section 4). Results are summarized in section 5.

2 Methods

2.1 Marine Radar

As a natively spatio-temporal measurement, MR is the ideal sensor for measuring wave dispersion in the field. MR maps wave energy on a dispersion surface and thus clearly discriminates between the free wave and nonlinear contributions. The MR wavenumber measurements are based on an iterative best fit of the dispersion surface to the observed wave signal that accounts for near-surface vertical current shear [*Lund et al.*, 2015]. Fig. 1 shows the results from MR covering ~160 hours worth of data that were collected during all major Arctic Sea State wave experiments (WE3, WE4, WE6, and WE7) from 11 Oct to 2 Nov 2015. The figure shows a total of 292 dispersion measurements, each of which corresponds to ~33 min of MR data. (The WE3 dispersion measurements have previously been reported in *Cheng et al.* [2017]). The surface waves observed by MR (up to a maximum frequency of 0.32 Hz) closely follow the linear dispersion relationship. The average deviation from linear dispersion as a function of frequency never exceeds ±0.2%, and for most frequencies 90% of measurements were within ±1% of linear dispersion. Based on hourly visual observations, the dispersion results show no systematic dependence on primary ice type. Since we have a high level of confidence in the MR results, they serve as the baseline for evaluating the success of the quality control measures designed for the buoy data.

2.2 Wave Buoys

The wave buoys were designed and built by author MD at Polar Scientific Ltd., and discussion of the design criteria and further technical details can be found in *Doble et al.* [2017]. Heave, pitch, and roll were output at 1 Hz and compass heading was output every minute. The heave was double integrated and high-pass filtered to give vertical displacement. Pitch and roll were integrated to give slope and combined with the compass heading to transform from a buoy reference frame to an Earth reference frame. The time series, vertical displacement and Earth referenced slope, were split into 30 minute blocks for spectral

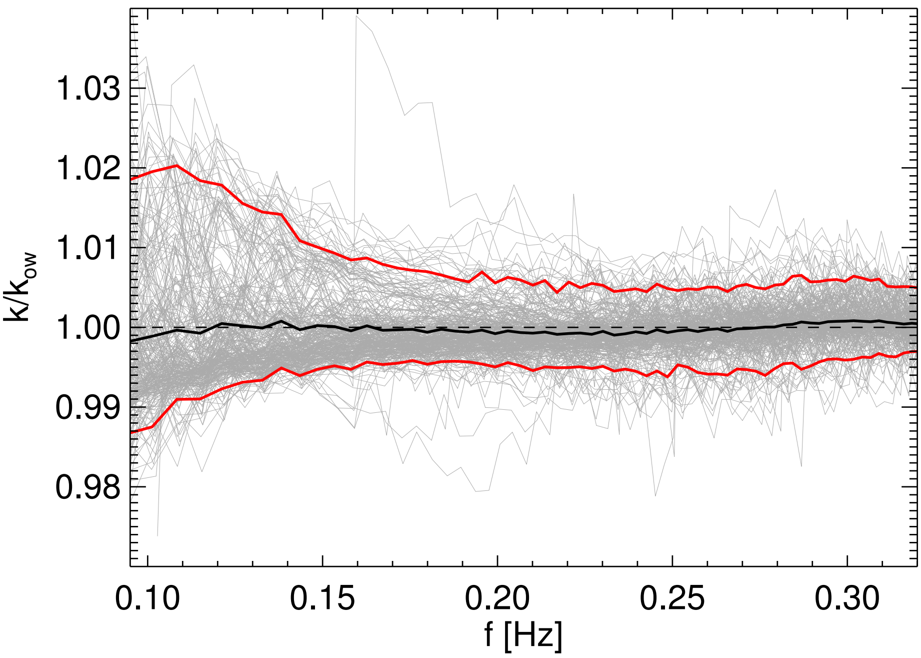

Figure 1. Ratio of MR-measured and open water wavenumber as function of frequency covering all Arctic Sea State wave experiments. The solid black curve corresponds to the mean value at each frequency, the red curves enclose 90% of measurements Arctic Sea State wave experiments

processing via fast Fourier transform (FFT). Individual spectral bands were averaged into 42 frequency bands which span the range 0.06 - 0.50 Hz.

2.2.1 Measurement Theory: Slope Correlation

A concise review of measurement theory can be found in *Krogstad and Trulsen* [2010], and the most relevant parts are summarized here. The most general representation of the sea surface is that of a stochastic field [*Barstow et al.*, 2005]. In this paradigm, all statistical information is contained in the wavenumber-frequency spectrum, $E(\boldsymbol{k}, \omega)$, the measurement of which requires a spatio-temporal observation such as MR.

When the sea surface is stationary, homogeneous, and ergodic, quantities which are measured as a time series at a point (e.g. pressure, slope, velocity, or acceleration), $X(x,t)$, are related to the wavenumber-direction spectrum via transfer function, T_X.

$$X(x,t) = \int_{\boldsymbol{k},\omega} T_X(\boldsymbol{k},\omega) e^{i(\boldsymbol{k}x - \omega t)} dE(\boldsymbol{k},\omega) \tag{2}$$

A triplet of these quantities can give a low order estimation of the directional-frequency spectrum, $E(f,\theta)$ [*Longuet-Higgins*, 1963; *Barstow and Krogstad*, 1984; *Young*, 1994; *Krogstad and Trulsen*, 2010]. The WBs follow the surface and measure heave, pitch, and roll (i.e. the vertical acceleration and two orthogonal angular rates) which result in records of surface elevation and slope in two orthogonal directions (η, $\frac{d\eta}{dx}$, $\frac{d\eta}{dy}$). These are a special subset of triplets which have transfer functions $(1, ik_x, ik_y)$ that do not invoke linear wave theory. The moments of the directional-frequency spectrum are

$$a_n + ib_n = \frac{1}{\pi}\int_0^{2\pi} e^{in\theta}E(f,\theta)d\theta \tag{3}$$

For convenience, we designate the triplet of quantities with the subscripts (1-3). From Eq. 2, the co- and quadrature spectra are related to the directional spectrum as follows.

$$C_{11} = \int_0^{2\pi} E(f,\theta)d\theta \tag{4}$$

$$C_{22} = \int_0^{2\pi} k^2\cos(\theta)^2 E(f,\theta)d\theta \tag{5}$$

$$C_{33} = \int_0^{2\pi} k^2\sin(\theta)^2 E(f,\theta)d\theta \tag{6}$$

$$C_{23} = \int_0^{2\pi} k^2\cos(\theta)\sin(\theta)E(f,\theta)d\theta \tag{7}$$

$$Q_{12} = \int_0^{2\pi} k\cos(\theta)E(f,\theta)d\theta \tag{8}$$

Rearranging these terms gives

$$k_e = \sqrt{\frac{C_{22}+C_{33}}{C_{11}}} \tag{9}$$

Where the subscript e indicates that the wavenumber is an estimate derived from buoy measurements. The first five Fourier coefficients of the directional-frequency spectrum are as follows

$$S(f) = a_0 = C_{11} \tag{10}$$

$$a_1 = \frac{Q_{12}}{C_{11}k} \tag{11}$$

$$b_1 = \frac{Q_{13}}{C_{11}k} \tag{12}$$

$$a_2 = \frac{C_{22}-C_{33}}{k^2} \tag{13}$$

$$b_2 = \frac{2C_{23}}{k^2} \tag{14}$$

In the coefficient definitions, k is either assumed to be k_{ow} or the form calculated from the auto-spectra by substituting in Eq. 9. When the form in Eq. 9 is inserted, one arrives at the normalized directional Fourier coefficients of Long (1980). Eq. 9 first appeared in the discussion of *Longuet-Higgins* [1963]. The interpretation is that k_e is a root-mean-square estimate of wavenumber

$$k_e = k_{RMS} = \langle k_x^2 + k_y^2\rangle^{\frac{1}{2}} \tag{15}$$

In the linear approximation, the magnitude of k depends only on frequency f, therefore $k_e = k_{ow}$. Generally though, waves are weakly nonlinear. The nonlinearity contributes to energy off the linear dispersion surface and in nonlinear, directionally spread seas, there is not an exclusive $f - k$ relationship [*Herbers et al.*, 2002; *Barstow et al.*, 2005]. However, theory and observations have revealed some important aspects of the structure of the nonlinear contributions. Contributions from second order spectra, i.e. wave sum and difference contributions, tend to dominate below the spectral peak, f_p, and sometimes dominate in the high frequencies beyond $4f_p$. Below f_p, this results in a marked increase of k, and when nonlinear contributions are dominant in the high frequencies, this results in a reduction of k [*Krogstad*, 2002; *Krogstad and Trulsen*, 2010; *Leckler et al.*, 2015]. Therefore, for k_e to represent free waves, a lower bound bound must be set to f_p, but there is no predetermined upper bound.

The $f - k$ relationship is Doppler shifted in the presence of currents [*Hauser et al.*, 2005; *Collins III et al.*, 2017a,b], but currents are a non-issue in our study. The MR deals with currents as an inherent part of the routine processing [*Lund et al.*, 2015]. The buoys were deployed as Lagrangian floats and thus measure the wave field in the frame of reference of the mean surface current. Although sometimes other factors influence the trajectory of a surface float, it was shown that our buoys closely follow the surface current (or sea ice) [*Lund et al., this issue*].

2.2.2 Quality Control

If Eq. 9 is to represent the dynamics of free surface waves, it must be assumed that the motion of the buoy perfectly follows the ocean surface for the range of frequencies measured. In this way, deviations of k_e from the open water relation have, in open water cases, been used as a quality control measure and as a flag for buoy response to currents, mooring forces, and bio-fouling [*Tucker*, 1989; *Tucker and Pitt*, 2001; *Thomson et al.*, 2015].

k_e is a simple combination of auto-spectra. Therefore, if one or more of the inputs, i.e. elevation and slope spectra, are noisy or dominated by nonlinear contributions the estimate of wavenumber will not reflect the free waves. When each auto-spectrum gives a definite signal, the frequency bands are subject to a confidence interval that is based on the number of degrees of freedom put into the χ^2-distribution. This sampling variability is propagated through the Eq. 9.

Fig. 1 shows that there was no change to wavenumber in the low frequencies up to ~0.30 Hz. Above 0.30 Hz, if deviations from open water occur, the expectation is that they will be small and increase as function of frequency. Pure mass loading represents the theoretical limit of the increase in wavenumber. At the highest measurable frequency, 0.50 Hz, there could theoretically be a maximum increase of 42% assuming 1/3 m ice thickness and 100% ice concentration. Deviations of another character, e.g. an order of magnitude different from open water, are a sign of noisy auto-spectra and can be dismissed.

2.2.2.1 Quality Control at the Block Level: QC1 In addition to an expected magnitude of deviation of k, the wave frequency spectrum, $S(f)$ has an expected form, particularly for wind seas, which have a high frequency face that decays with f^{-4} [*Donelan et al.*, 1985; *Toba*, 1973]. Thus, the spectral form can be used to identify spurious spectra. The WBs were subject to a number of events that effected the calculation of spectra and wavenumber: data collection initiated while on deck of the ship or was ongoing during deployment or recovery, they flipped upside-down and righted, they were subject to significant icing, and their motion was obstructed or impacted by ice floes. A number of these events were noted in an event log during the experiment, but since the buoys operated autonomously, there were certainly some events that were overlooked. Any one of these events influence the free motion at the surface, and, with the exception of light icing, would have resulted in $S(f)$ with unrealistic shapes and k_e orders of magnitude different from the open water relation. Therefore, odd shapes of spectra and large deviations of k_e from k_{ow} were an indication of noise or obstruction of buoy motion. These spurious spectra were particularly suspect if they are isolated in time with adjacent spectra that were acceptable.

The first level of quality control, referred to as QC1, was a binary pass or fail for each 30-minute block based on the frequency spectra and normalized wavenumber-frequency relationship. QC1 was performed by visual inspection of $S(f)$ and k_e/k_{ow}, and corroborated with the buoy event logs when possible. Of the initial 1108 blocks, 724 passed QC1.

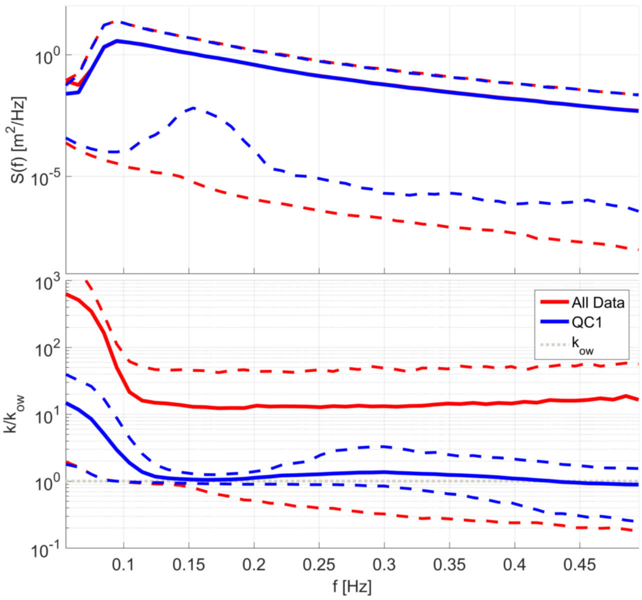

Figure 2. Top panel) Wave frequency spectra with mean in solid line and interval containing 90% of the data in dashed line. All data in red, QC1 data in blue. Bottom panel) Same for normalized wavenumber, k_e/k_{ow}.

Figure 2 shows the means and intervals containing 90% of the data for the $S(f)$ and k_e before and after QC1. The mean of the $S(f)$ did not significantly change, but the lower bound of the interval containing 90% of the data increased substantially. This means that most of the data that failed QC1 possessed very low energy. The normalized wavenumber lowered from an average above 10 to closer to 1 for the range of frequencies greater than 0.10 Hz. The interval containing 90% of the data reduced substantially (from ~3 orders of magnitude to < 1 order of magnitude for $f > 0.10$ Hz), but scatter remains particularly for the range of frequencies lower than 0.10 Hz and larger than 0.25 Hz. The next analysis is performed to better understand the remaining variability in k_e and further refine estimates of k_e.

2.2.2.2 Signal and Noise Characterization Following QC1, there were 724 blocks which Table 1 breaks down by deployments.

Wave and ice conditions for each deployment have been noted elsewhere [*Wadhams and Thomson*, 2015; *Cheng et al.*, 2017; *Thomson et al.*, 2017]. After examining each of the individual deployments, it became apparent that there were good and bad bands within some 30-minute frequency spectra. This is a result of the combination of nonuniform signal to noise ratios across frequencies and the dominance of nonlinear contributions in some bands. To get an idea of the character of the signal across frequency bands, we set an absolute threshold, first constant and then variable in frequency, and examined the change in the shape of the mean and standard deviation (*std*) of k_e/k_{ow}. Because there is so little varia-

Table 1. Name of each deployment, number of buoys, number of good data blocks, and parameters y and m for Eq. 17

Deployment	No. of Buoys	No. of Blocks	y	m
Wave Experiment 1	1	3	n/a	n/a
Wave Experiment 2	1	8	n/a	n/a
Wave Experiment 3 (group 1)	2	41	6.8129e-5	7.6753
Wave Experiment 3 (group 2)	5	171	6.8129e-5	7.6753
Wave Experiment 4	6	31	n/a	n/a
Wave Experiment 6	5	235	n/a	n/a
Wave Experiment 7	6	235	3.5672e-8	29.1393
total	26	724		

tion in the normalized wavenumber observed by MR in Fig. 1 (up to ~0.30 Hz), it can be assumed that most of the variation in k_e is a result of the influence of noise or nonlinear contributions. Therefore a decrease in (*std*) can be interpreted as sign of increased signal.

Absolute Noise Threshold Constant in Frequency Here an absolute noise (i.e., minimum energy) threshold, constant across frequency, was set and then applied to each spectrum. The mean and *std* are shown for the resulting normalized k_e. Both the mean and *std* decreased as a function of increasing threshold, which means that as the threshold increases the signal to noise ratio improves. Starting with the lowest threshold, the mean normalized k_e starts off high then approaches 1 at 0.15 Hz, it again increases starting at 0.20 Hz and peaks at a value of 1.3 near 0.27 Hz. It slowly and continuously decreases from 0.3 Hz, crossing below a value of 1 at 0.42 Hz. The *std* is high (> 0.2) except for a small range around 0.15 Hz. The effect of an increasing threshold is to make the mean converge to much closer to 1 and extend the lower range of frequencies with values near 1, the *std*s also become uniformly smaller with most of the frequency range under a value of 0.1.

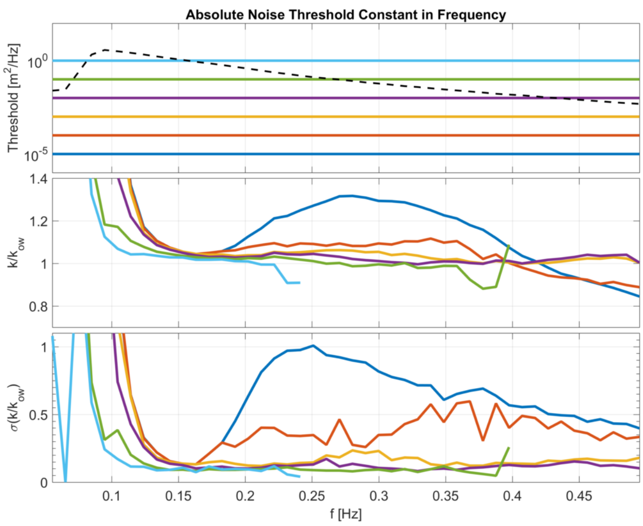

Figure 3. Top panel: different thresholds in color with the mean wave spectra in dashed black. Middle panel: resulting normalized wavenumber, corresponding to each threshold, shown in color. Bottom panel: the *std* of normalize wavenumber for each threshold.

With increasing threshold, k_e/k_{ow} approaches a value of 1 across the board except at frequencies > 0.40 Hz, where the values are slightly increased. With the highest two thresholds, the high frequency information gets cutoff due to the characteristic decay of energy in the high frequencies. To further investigate the behavior at high frequencies, we choose an alternate shape of threshold, based on the shape of a baseline noise spectrum of the buoys, which preferentially allows more high frequency energy.

Absolute Noise Threshold Variable in Frequency To determine a baseline noise spectrum, a quiescent period was identified. During this period there was almost no detectable wave energy, the average significant wave height over 7 hours was 0.01 m, well under the minimum accuracy [*Doble et al.*, 2017], thus the resulting spectrum was dominated by noise. The mean spectral shape over this 7 hour period, which decays from low to high frequencies, serves as the basis of a threshold. The result with mean and *std* for the normalized k_e was similar to 3 across the range of frequencies. The mean of k_e/k_{ow} approaches 1 for all frequencies except for the highest range of frequencies, above 0.40 Hz, which show a slight increase in value.

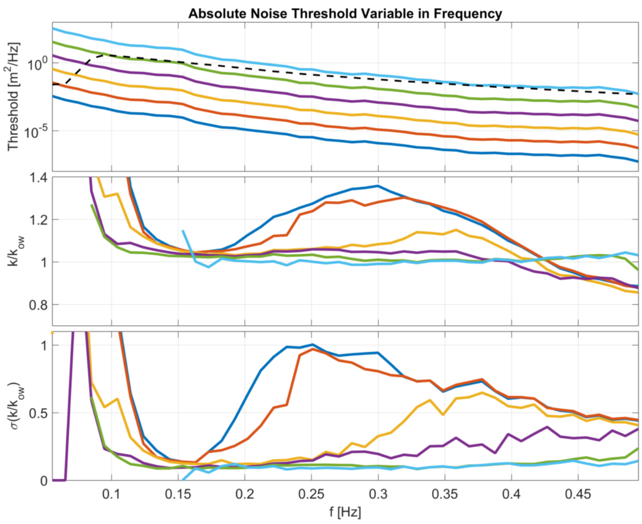

Figure 4. Same as Fig. 3 for thresholds which decrease as a function of frequency.

The results in Figures 3 and 4 are encouraging in that they confirm expectations about the character of normalized k_e: it is close to a value of 1 over the whole range of frequencies with perhaps slight deviations confined to the high frequencies. There is also an indication that the deviations of k_e from k_{ow} match our understanding of the nonlinear contributions; over most of the frequency range there is an increased value of normalized k_e, but in the high frequencies the value decreases. The nonlinear contributions appear to have dominated outside of the energy containing region of the spectrum. Therefore, a threshold independent of the amount of energy in a given wave spectrum is not appropriate for characterizing k_e. Instead, we proceed with the threshold which is set relative to the value of $S(f_p)$.

2.2.2.3 Relative Threshold: QC2 QC1 refined the data to cases with spectra which, at least within some bands, gave spectra and k_e with more signal than noise. Secondary quality control, QC2, is aimed at isolating bands of free wave signal within each spectrum. Unlike QC1, there is no evaluation of the departure of k_e from the linear dispersion. We avoided this type of criterion because, in the end, k_e is the signal we wish to interpret, and it would be all too easy to design a criterion, even unintentionally, which gives a shape that meets our hypothesis.

QC2 involves defining a threshold for each spectrum. The threshold is based on the level of the spectral peak, $S(f_p)$, for each individual spectrum. A function is defined which decays like f^{-d} and is set by one additional parameter, a scalar, n_p, which offsets the function at f_p a certain percentage of $S(f_p)$. So, per spectrum, the threshold equation is the following:

$$S(f) \geq \frac{n_p \times S(f_p)}{f_p^d} f^d \tag{16}$$

The parameter d was chosen to be 5.3, based on a fit to the noise spectrum used in section 2.2.2.2. It was found that the shape of mean k_e is not sensitive to this number as long as the decay rate is faster than expected for wind seas, i.e. $d \leq 4$. The results are not very sensitive to the choice of this n_p, here, 0.25 was chosen. The main effect of this threshold is to filter out the data in frequencies below the peak frequency, and hence the nonlinear contributions which tend to dominate there. In general, this approach is well suited to different shapes of spectra including bi-modal spectra. In bi-modal cases, if the peak corresponds to the lower of the two modes, both areas of energy tend to pass the threshold while bands in-between are cut. However, when the peak corresponds to the higher frequency mode, the threshold cuts out the lower frequency mode. In this way, the approach is not perfect.

Eq. 16 is combined with another criterion designed to remove data which were below an obvious noise floor. This noise floor only appeared in the high frequencies and only during three deployments, wave experiment 3 (groups a and b) and wave experiment 7. The shape of this noise floor can be described by the following function,

$$S(f) \geq y e^{mf} \tag{17}$$

The values for parameters y and m are given in Table 1.

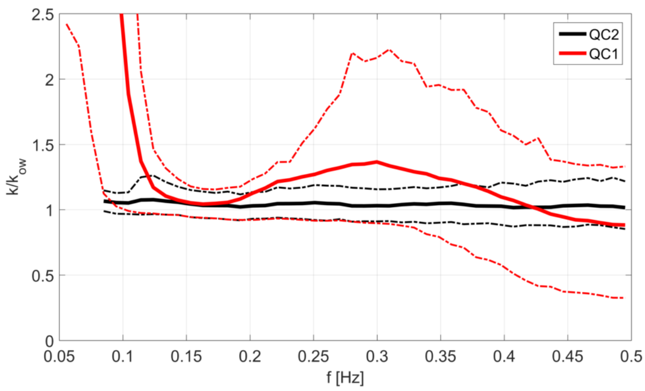

Figure 5. Normalized wavenumber as a function of frequency. Solid line is mean, dashed lines show the upper and lower bounds containing 90% of the data. Red is data following QC1. Black is data following QC2.

Figure 5 shows the results from QC1 and the additional refinement due to the application of QC2. Again, the deviations of k_e/k_{ow} from 1 in the QC1 data are consistent with nonlinear contributions to k: a drastic increase in the very low frequencies and slight decrease in the high frequencies. Compared with QC2, the upper bound of the interval containing 90% of the data is significantly increased in the range 0.25 - 0.40 Hz, and the the lower bound is significantly decreased in the high frequencies starting around 0.35 Hz. The mean of k_e/k_{ow} in the mid-frequencies is also increased from 1 to a maximum of ~1.3. This is most likely due to times when the peak frequency is shifted up in frequency introducing nonlinear contributions in the range of frequencies below the peak. Figure 6 shows that most spectra have f_p in the range of 0.10 - 0.20 Hz, but there are also a number of spectra with f_p in the range of 0.25 - 0.35 Hz, and none above 0.40 Hz. In Fig. 5, the mean of QC1 crosses 1 around 0.43 Hz, where, ostensibly, there were no lower-than-the-peak nonlinear contributions because none of spectra have their peak in that range.

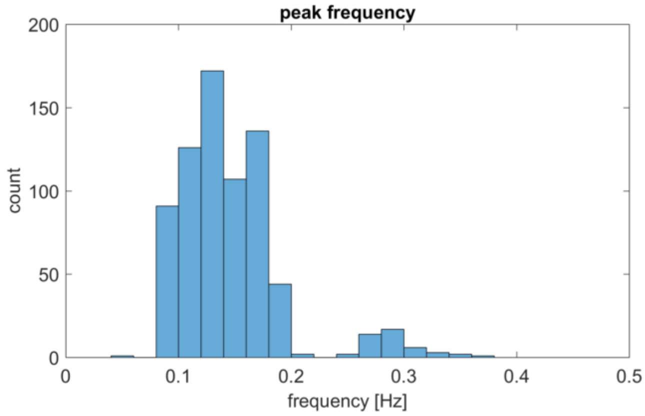

Figure 6. Histogram of peak frequencies.

In Fig. 5, means and 90% data intervals of post QC1 and post QC2 data overlap only over a small range of frequencies centered around 0.15 Hz. Fig. 7 shows details of the mean and interval containing 90% of the data for k_e/k_{ow} following QC2. No data remain from 0.05 - 0.08 Hz, in the ranges of 0.09 - 0.13 Hz and 0.20 - 0.40 Hz the mean k_e/k_{ow} is reduced, and from 0.45 - 0.50 Hz it is increased. So, the k_e/k_{ow} is much closer to 1 over the range of 0.09 - 0.50 Hz with much more uniform variability. Apparently, QC2 was effective in removing most of the nonlinear contributions to k_e, though it is likely that some nonlinear contributions still remain.

The mean k_e/k_{ow} is consistently above 1. On average the deviation from the open water relation is 4% increased and 70% of the data lie within 10% of k_{ow}. This variability is at least an order of magnitude greater than the MR observations. There is a maximum in the low frequencies centered around 0.12 Hz, and 3 smaller peaks around 0.25, 0.35, and 0.47 Hz. The upper bound of the interval containing 90% of the data has a corresponding drastic increase around 0.12 Hz, hits a minimum around 0.20 Hz, and then increases steadily. The lower bound decreases, almost linearly, from 0.99 to 0.85 from 0.09 - 0.50 Hz.

Theoretically, if the normalized wavenumber deviates from 1, deviations should be strongest in the high frequencies. In Fig. 7 the mean deviation from 1 decreases in the high frequencies. The deviations in the low frequencies have corresponding increased variability. In addition, the MR data in Fig. 1 indicate that the mean normalized wavenumber, from 0.10 - 0.32 Hz, was ~1 with 90% of the data falling within 1% of k_{ow}. For these reasons, the increases centered around 0.12, 0.24, and 0.35 Hz are likely artefacts of remaining nonlinear contributions. Next we explore a high wave energy subset of the data.

2.3 Wave Experiment 3

To further avoid nonlinear contributions, we restrict analysis to a single deployment, WE3 (group b). WE3 was a high-energy wave event characterized by single-peaked wind seas with f_p around 0.10 Hz, a scenario under which we expect nonlinear contributions in the low frequencies to be confined below 0.10 Hz. The wave event spanned 3 - 4 days from

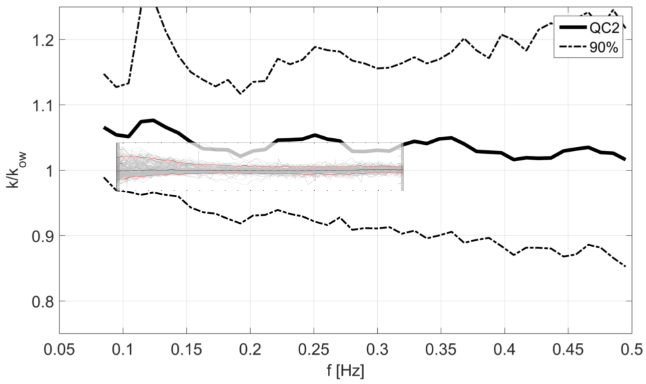

Figure 7. Detail of QC2 data from 5. Normalized wavenumber as a function of frequency. Solid line is mean, dashed lines show the upper and lower bounds containing 90% of the data. Also shown are MR data in gray with 90% data intervals in red.

10 Oct. 2015 to 13 Oct. 2015. During this time a couple of WBs (group 1) were deployed at an initial site which was abandoned once satellite imagery revealed a rapidly vanishing fetch [*Wadhams and Thomson*, 2015]. Based on fetch estimates from the satellite images, a second deployment (group 2) was deployed to strategically sample the largest possible waves. The group 2 dataset included 171 spectra from 5 WBs: WB2, WB3, WB4, WB5, and WB7. The buoys were deployed in an array which was more or less aligned with the wind and wave direction. The ice during this time was loose, thin ($\leq$ 0.3 m) pancakes with a matrix of brash ice in-between floes. This event is well described in several other places [*Collins III et al.*, 2017b; *Rogers et al.*, 2016], please refer to these and other articles in this special issue for more information.

We simplify the first criterion of QC2 by dismissing all data below f_p. The spectra and resulting mean and interval containing 90% of the data are shown in Fig. 8. Due to the high energy, the filtered data were confined to the frequencies below the peak and some of the low energy, high frequency data. For k_e/k_{ow}, there was a removal of data in the low frequencies, and in the high frequencies the mean was shifted from slightly below 1 to slightly above 1. The lower bound of the 90% interval is greatly reduced in the high frequencies. Between 0.15 and 0.30 Hz, k_e is within 1% of k_{ow}, but exceeds this in the lower and higher frequency ranges. It is likely that the low frequency departure is an artefact of imperfect filtering, but the deviation in the high frequencies cannot be dismissed as easily.

Surprisingly the variability, relative to the MR data, remains high. The variability of k_e, as represented by the 90% data interval, did not significantly decrease compared to the overall post QC2 dataset except for the upper bound at 0.12 Hz which decreased from 1.26 to 1.12. In fact, both bounds increased from the overall data for frequencies greater than 0.35 Hz. Since the sampling variability was similar for the overall experiment and the subset, the increased variability in the high frequencies might be a sign of variability in the ice conditions encountered.

Proceeding with the filtered data from WE3, we examine the small scale, space-time variations in k_e/k_{ow}.

3 Results from WE3

The deployment of WBs in WE3 lasted a little over 2 days, from 11 October 2015 07:30:00 UTC to 13 October 2015 09:30:00 UTC. Due to the different deployment and re-

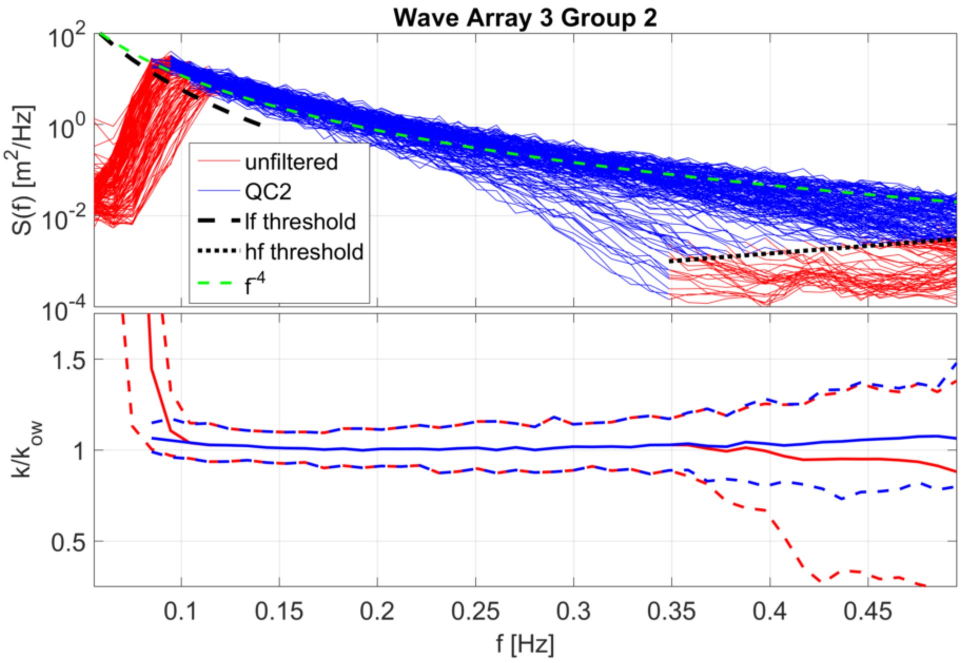

Figure 8. WE3 data. Top panel: frequency spectra with data which passed QC2 in blue and data that failed in red. The dashed green line is proportional to f^{-4}. The dashed black line shows an example of the curve given by Eq. 16 called lf threshold (not used for WE3) and the dotted line shows Eq. 17 called hf threshold. Bottom panel: normalized wavenumber and upper and lower bounds of interval containing 90% of data.

covery times, and some loss of data from overturned buoys and loss of heading signal, the records for each buoy are intermittent and cover different time periods recorded in Table 2.

Table 2. Name of each buoy, number of blocks, and ice concentration

Buoy Name	No. of Blocks	start	end	ice concentration[a]
WB2	3	12 Oct. 02:30	12 Oct. 03:30	6.2
WB3	42	11 Oct. 09:30	12 Oct. 10:30	5.1
WB4	27	12 Oct. 00:00	12 Oct. 13:00	63.0
WB5	48	11 Oct. 07:30	12 Oct. 11:00	32.4
WB7	51	11 Oct. 11:00	13 Oct. 09:30	0.7
total	171			

[a] mean along buoy path of interpolated ice concentration from AMRS2

3.1 Mean k_e

Fig. 9 shows the mean wave spectra and normalized wavenumber (k_e/k_{ow}) for each of the buoys deployed during WE3 (solid lines), with the interval containing 90% of the data (dashed lines). Each 30 minute estimate used for these means are given in video form in the supplemental material. The buoys drifted with the sea ice (or surface currents) towards the west-north-west, approximately in the direction of the wind and waves. The map of buoy deployment locations also shows the mean ice concentration (i.e. fractional surface coverage) over the deployment period, which was calculated from a 24-hour AMSR2 product. The ice concentration varied in time. Although the overall trend during the autumn is ice advance from the north, this storm caused a temporary retreat of ice (due to both advection and melting [*Smith et al., this issue*]). A large tongue of ice can be seen extending to the south east from an area of high concentration centered around 73° N 154° W. The mean ice concentrations along each buoy path can be found in Table 2. WB3-5 clearly encountered higher ice concentration than WB7, which was primarily in open water. WB2, only had 3 spectra and although it furthest along the array, it seems to have been deployed in pocket of low ice concentration. Wave spectra of WB7 was higher than other buoys at all frequencies, and the k_e/k_{ow} remains near one. In comparison, wave spectra of WB2-5 are damped, and k_e/k_{ow} are higher than one above 0.30 Hz.

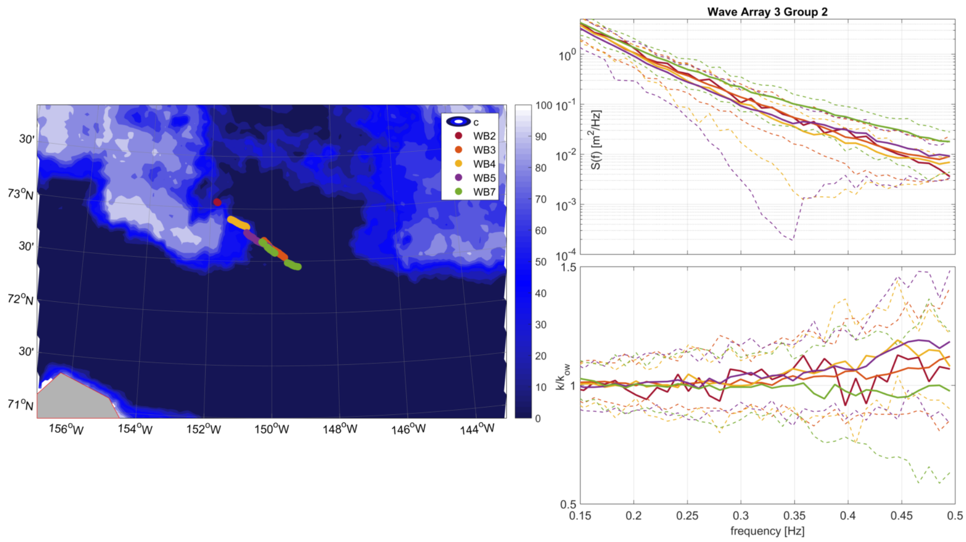

Figure 9. Time-averaged wave data from WE3. Left panel: map of experiment area with ice concentration, from AMRS2, in cool color contours and the paths of the WBs in bright color circles. Right top panel: mean and interval containing 90% of frequency spectra. Right bottom panel: mean and interval containing 90% of normalized wavenumber.

3.2 Temporal variation of k_e

The means shown in Fig. 9 obscure temporal variations in wave conditions. Due to the innate sampling variability, it is difficult to track coherent deviations of normalized wavenumber. Fig. 10 shows k_e/k_{ow} as a function of f and time. WB3,4, and 5 show an increase in the high frequencies from 12 Oct. 18:00 - 13 Oct. 12:00, and WB7 shows a significant decrease near the beginning of its times series for about 6 hours. Unfortunately, the high frequency wave information was filtered, particularly in the beginning of the time series for WB5 and towards the end of the time series for WB4. All WBs show a slight increase over all frequencies with time.

To examine any temporal trends, we subtract out the open water wavenumber and take the mean over the frequency axis (Fig. 11). The figure shows the mean deviation from open water dispersion across all frequencies > 0.15 Hz. There is a clear increasing trend for all buoys (except for WB2, which had too few data points). Although the WBs and ice are thought to drift together [*Lund et al., this issue*], an upward trend in wavenumber would seem to indicate that the buoys were going deeper into the MIZ and hence encountering thicker and higher concentrations of ice with time. However, as the ice was retreating during this storm, the ice concentration along most WB paths appear to decrease over time. The excep-

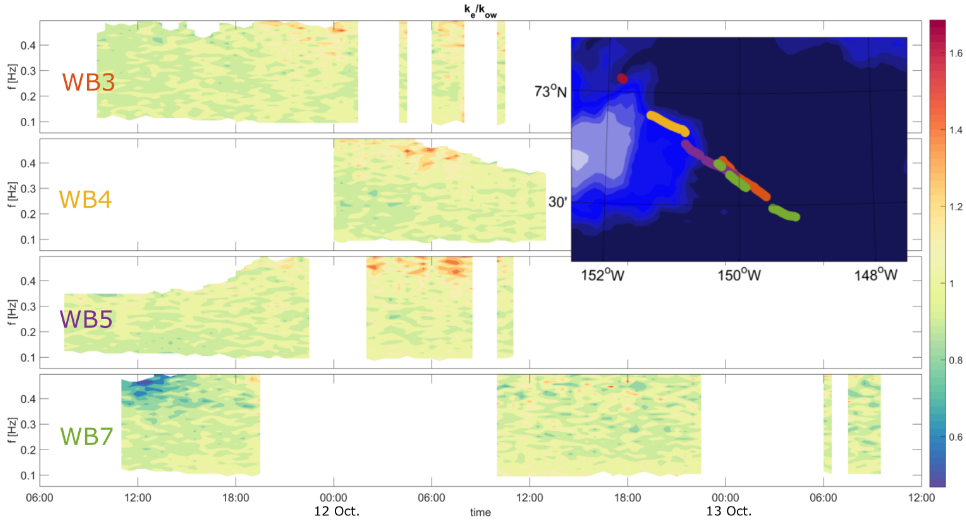

Figure 10. k_e/k_{ow} shown in color contours as a function of frequency and time for WB3, WB4, WB5, and WB7. Inset: a map with the buoy paths and mean ice concentration contours.

tion is a discontinuous jump for WB4 and WB5 where they are overtaken by a patch of high ice concentration (a non-physical artifact of the arrival of an updated AMRS 2 image at 12 Oct. 00:00), but then they continue the downward trend.

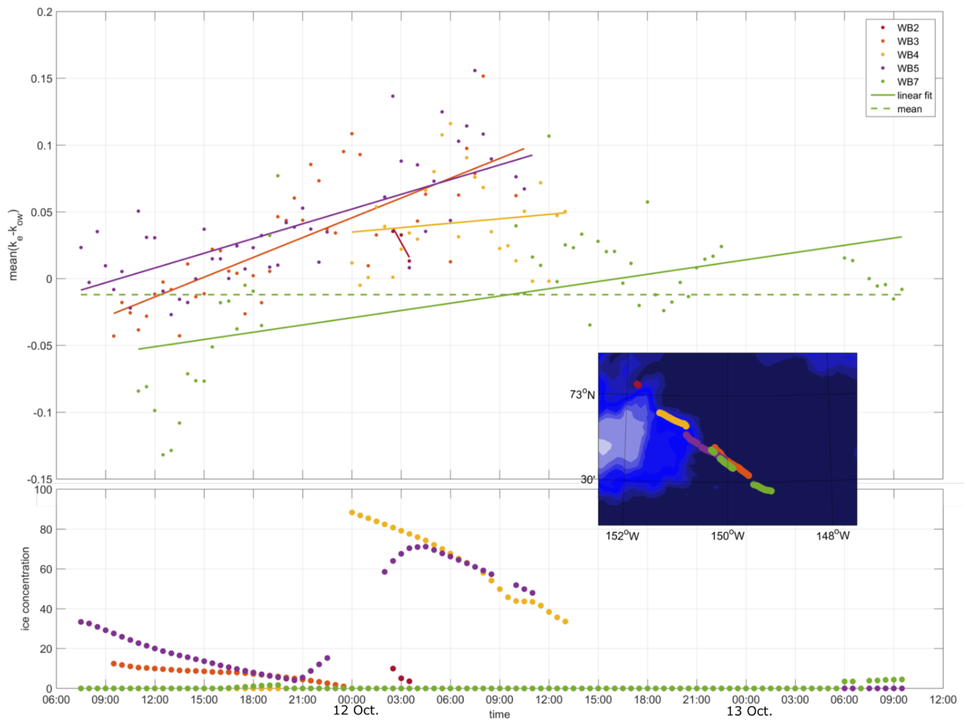

Figure 11. Top panel: Mean difference of k_e from k_{ow} as a function of time in colored dots with a linear fit in solid lines. Also shown is the mean of WB7 with dashed green line. Bottom panel: ice concentration inferred from 24 H AMSR2 product as a function of time. Inset: a map with the buoy paths and mean ice concentration contours.

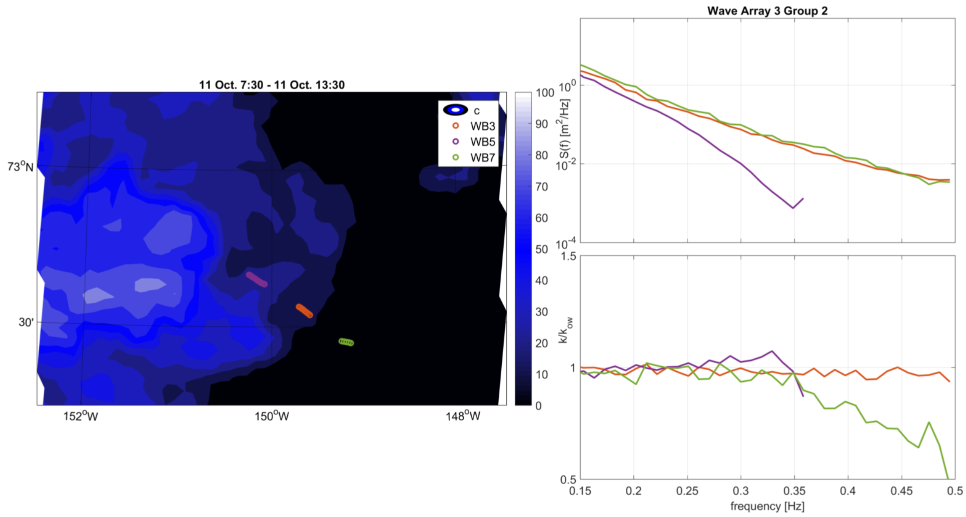

Figure 12. Time-averaged wave data from WE3 from 6 hours of data during WE3, 11 Oct. 2015 07:30:00 to 11 Oct. 2015 13:30:00. Left panel: map of experiment area with ice concentration, from AMRS2, in cool color contours and the paths of the WBs in bright color circles. Right top panel: mean of frequency spectra. Right bottom panel: mean of normalized wavenumber.

Fig. 12 shows mean wave data over 6 hours, from 11 Oct. 2015 07:30:00 UTC. The map indicates that the buoys encountered increasing ice concentrations at this time, from 0% at WB7 to 10% at WB5 to 20% at WB3. It appears that estimates of k_e/k_{ow} from WB7 dips below 1 consistently in the high frequencies, with a deviation that increases as a function of frequency. Since this buoy is most likely in open water, and the frequency range is $3-5f_p$, it is possible that this decrease in wavenumber is a reflection of the dominance of harmonics. If this decrease was caused by ice, it would be reasonable to expect to observe similar deviations in the other buoys, which are not apparent. The mean spectra from WB5 and WB7 overlap, indicating that in terms of attenuation, there was not enough distance of ice between the two to strongly attenuate waves, but k_e from WB5 is increased compared with WB7 and has near perfect agreement with k_{ow}. If WB7 was observing harmonics, then they appear to have been suppressed by the lightly concentrated ice surrounding WB5. However, this decrease of wavenumber for WB7 was not persistent in time as seen in Fig. 10. One can conjure a physical explanation consistent with harmonics, such as WB7 encountering increased ice cover. However, it is possible the deviation is an artifact of some unknown interference to buoy motion early in the experiment. WB5 energy is significantly damped and the spectra dip below the threshold set for the high frequencies. In contrast to the other buoys, k_e/k_{ow} for WB5 appears elevated from 0.25 - 0.32 Hz before dipping at the cutoff.

Fig. 13 shows another 6 hour average a day later. Again, the WB with the highest energy mean spectra was WB7, with the remaining mean spectra displaying damping which reflects the buoys' depth into the ice cover. Mean spectra of WB7, WB5, and WB3 are close in energy, but WB4 is significantly damped. However, in the plot of k_e/k_{ow}, the WB7 curve for $f > 0.35\ Hz$ is clearly lower than the ones for the other 3 WBs. This is not contradictory, as the shape of k_e is indicative of the wave response to local ice properties whereas attenuation has a spatial component. I.e., ice may have similar characteristics in 3 places resulting in the 3 similar shapes of k_e (and local attenuation rates) while total attenuation is a function of distance and integrated over all ice previously encountered. Nevertheless, the map of ice concentration indicates that WB4 encountered significant higher concentrations of ice which is not reflected in the observations.

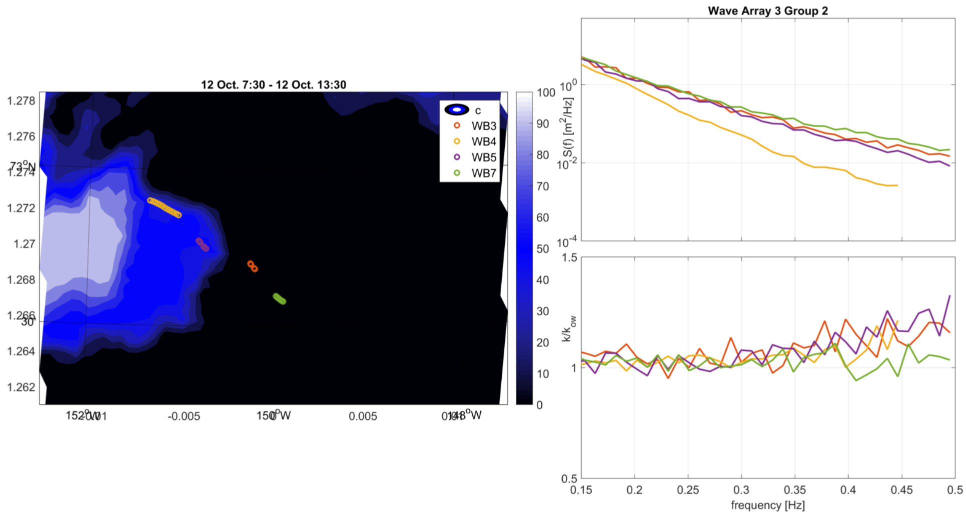

Figure 13. As in Fig. 12 for 12 Oct. 2015 07:30:00 to 12 Oct. 2015 13:30:00.

4 Discussion

The results from WE3 show small deviation from linear dispersion confined to the high frequencies (> 0.30 Hz). In this region, there is an increase in wavenumber that becomes larger as a function of frequency. These findings are similar to those of *Fox and Haskell* [2001], and are consistent with the theoretical effect of mass loading.

The mass loading model [*Weitz and Keller*, 1950; *Squire*, 1993], is given as

$$k_{ML} = \frac{(2\pi f)^2}{g - c\rho_{ice}h(2\pi f)^2/\rho} \tag{18}$$

In this formula, g is acceleration due to gravity, c is ice concentration, h is ice thickness, ρ is the density of sea water (1025 kg/m^3), ρ_{ice} is the density of ice (here assumed to be 0.9ρ). The effect of mass loading depends on the volume of ice in the surface layer, which is separated into two components: ice concentration and ice thickness [*Wadhams and Holt*, 1991]. If the ice thickness does not vary over a given area, then dispersion is primarily controlled by concentration.

In Figure 14, we compare the mean k_e/k_{ow} for 5 WBs and a combination of buoys (WB3, WB4, WB5) excluding WB2 which only had 3 data points from a pocket of low ice concentration, and WB7 which was near or in open water. The results of the mass loading model for an ice thickness of 1/3 m and for concentrations from 0 - 100%. Also shown are intervals containing 90% of the WB time averages. The increase of wavenumber for individual WBs is qualitatively consistent with mass loading, and the corresponding concentrations are reasonable. However, the mean k_e values do not follow the same concentration contour across all frequencies. They tend to be close to k_{ow} until 0.30 Hz and then depart from k_{ow} more strongly than lower concentration k_{ML}s crossing several concentration contours.

The figure also shows a combination of 3 WBs which were centrally located in the array and have similarly shaped k_e curves. The average smooths out the variation between the 3. In the range of 0.15-0.28 Hz, the mean k_e appears to follow the 10% c contour. From 0.28-0.50 Hz, the mean appears to increase almost linearly from the 10% c contour to the 40% c contour. Remarkable, the shape of the upper and lower 90% intervals mimic the shape of the 100% and 0% contours, respectively. Perhaps the shape of k_e, which crosses concentration contours, indicates that other ice effects are important. Although it is difficult to ar-

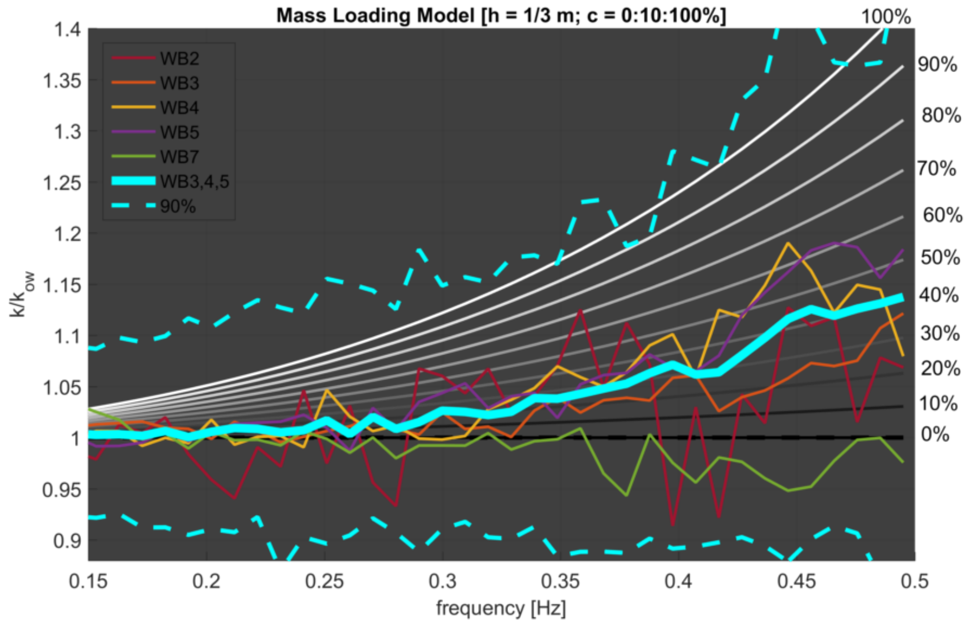

Figure 14. Normalized wavenumber as a function of frequency. The curves on a gray scale show the mass loading model for an ice thickness of 1/3 m and ice concentrations ranging from 0 - 100% with 10% contours. The colors show the time averages of the various buoys.

gue that elasticity effects are important in the ice type observed here, it is possible that there was some effective viscosity due to the presence of frazil ice between floes. Indeed, the results of *Cheng et al.* [2017] suggest significant values of effective viscosity which would alter the shape of dispersion in addition to ML (see Fig. 7 of *Cheng et al.* [2017] and Fig. 6 of *Collins III et al.* [2017a]).

The range of ice concentrations suggested by the mean of the 3 WBs, 10 - 40% c, is reasonable for the conditions observed. However, the 90% data interval encompassed the entire range of values possible with the mass loading model. Some of the variability in k_e is a reflection of the variable ice conditions, but it is impossible to ignore the innate sampling variability which was at least 10x higher than what was observed by the MR.

Collins III et al. [2017a] suggested that the successful use of the slope-correlation method will translate into routine measurements of k_e in icy conditions. However, our results indicate quality control is the most crucial step for ensuring that the k_e signal is representative of the free surface waves, and is not simply an artifact of buoy motion or nonlinear spectral contributions. The quality control developed in this study includes various steps, some of which require visual inspection. Such in-depth quality control would be challenging to implement on a routine basis. Even with careful quality control, the variability in buoy k_e requires a large number of measurements to be averaged to get a smooth result. As that number increases, the assumptions of stationarity and homogeneity are more likely to be violated. In the case of pure mass loading, one may be able to invert Eq. 18 for ice concentration with known thickness or ice thickness with known concentration [*Wadhams and Holt*, 1991]. This is most likely impossible to do with accuracy on the scale of individual spectra because of the data variability.

Time averaging of recorded buoy data may obscure the temporal variation of k_e and ice concentrations during each deployment. However, we find that the correlation between ice concentration, interpolated to the buoys' time step and location, and the mean deviation from k_{ow} along f was low ($R^2 = 0.40$). The low correlation is partially due to the sampling variability of k_e, but it may also reflect the deficiency of the daily AMSR2 ice concentration product for evaluating a quantitative model of dispersion. The daily product does not resolve the time and space scales needed to evaluate the time variation of buoy data. Evaluation of wave attenuation values during this study period indicated that the attenuation rate was not simply increasing as function of distance along the array, such that a linear interpolation between products is not appropriate. This is likely a result of variable ice concentration over the study region, as well as convergence of ice into small-scale bands as a result of surface current convergence zones *Lund et al., [this issue].* The concentration and thickness of ice in these bands is high compared to the surrounding seas. Higher resolution ice products of the region in which buoys were deployed would allow interpretation of the spatio-temporal variability of k_e.

Figure 15. An example of icing of a WB after recovery during the WE3 deployment.

Lastly, it should be mentioned that icing of the buoys was observed during this deployment. An example is shown in Fig. 15. *Thomson et al.* [2015] found that bio-fouling increases the mass and volume of their buoy overtime, which results in an increase of a metric called the check ratio in the high frequencies. Their check ratio was a measure of the ellipticity of the wave orbit, i.e. the ratio of the horizontal to vertical displacement. How an increased buoy mass and volume due to icing might affect slope response (vs. displacement response) is unknown, but their study suggests that it is possible that significant icing may alter the buoy response, particularly in the high frequencies. The exact amount of icing was not measured, but Fig. 15 shows a relatively thin layer of ice surrounding the buoy. Due to a relatively modest increase in terms of volume, the icing likely did not change the so called size-filtering effect of the buoy, where the highest frequency measured is limited to that of twice the buoy length [e.g., *Collins III et al.*, 2014]. While the difference in mass is unknown, its effect on our results would have been mitigated by the increase buoyancy of the ice on the underside of the buoy.

5 Summary

We present wavenumber data from shipboard marine X-band radar and Lagrangian wave buoys during the Arctic Sea State DRI with a special focus on wave experiment 3. The MR sampled along the ship track throughout various wave experiments and is an excellent sensor for measuring dispersion. The spatio-temporal measurement allows the mapping of wave energy onto a dispersion surface in wavenumber-frequency space. Using an iterative fit, the MR derives a dispersion relation which discriminates between linear and nonlinear contributions. Through this technique, we found that wave dispersion in ice matches exactly that of open water with 90% of the data within ±1% of k_{ow}. Unfortunately, the range of observable waves was limited to frequencies of 0.32 Hz and below. In this range, the MR confirmed our hypothesis of little deviation from the open water relation and served as a baseline for the buoy measurements.

Wavenumber was derived from the WBs using a slope-correlation technique [*Longuet-Higgins*, 1963]. Buoy wavenumber, k_e, was found to be very sensitive to noise and nonlinear contributions. Even with careful quality control, the variability in k_e was an order of magnitude higher than that of the MR. Wave experiment 3 had the strongest wave signal and was chosen for further analysis. During WE3, the MIZ was dominated by thin, loose pancake ice. WBs were deployed in an array aligned with the peak wave direction with the idea of sampling from near open water to deep into the MIZ. Averaging all buoy observations, the wavenumber matched that of the MR in the range of 0.10 - 0.30 Hz.

Excluding the buoy closest to open water, it was found that wavenumber increases from the open water relation for frequencies > 0.30 Hz. The deviation increased as a function of frequency. This finding is consistent with the mass loading effect of ice, and suggests elasticity is unimportant in the MIZ. This is intuitive as waves should not "feel" the elastic properties of loose floes with diameters much smaller than the characteristic wavelength. A comparison with the ML model with various ice concentrations gave a reasonable result of ice concentrations in the range of ~10-40% on average. However, the trends seem contradictory: wavenumber increased in time along the WBs' path whereas concentration (as inferred from a satellite product) mostly decreased. The mean of k_e, from several buoys centrally located in the array, crossed several ice concentration contours, perhaps suggesting effective viscosity was also at play, or that the buoy measurements were inadequate because the number of k_e measurements required to get a smooth average may have violated assumptions about stationarity and homogeneity.

Acknowledgments

Arctic Sea State was funded by ONR and managed by Martin Jeffreys and Scott Harper (MD grant N000141310290, BL through N000141310288, COC through N0001413WX20825, MS through N000141310284. This work was facilitated by all the Arctic Sea Staters under the leadership of Jim Thomson. COC thanks Erick Rogers for his guidance into the world of waves and ice and NRL for their sponsorship. All raw data available through Arctic Sea State data archive. Contact first author for any specific figures seen here.

References

Barstow, S. F., and H. E. Krogstad (1984), General analysis of directional ocean wave data from heave pitch roll buoys, *Modeling, Identification and Control*, *5*(1), 47.

Barstow, S. F., J.-R. Bidlot, S. Caires, M. A. Donelan, W. M. Drennan, H. Dupuis, H. C. Graber, J. J. Green, O. Gronlie, C. Guérin, et al. (2005), Measuring and analysing the directional spectrum of ocean waves.

Cheng, S., W. E. Rogers, J. Thomson, M. Smith, M. J. Doble, P. Wadhams, A. L. Kohout, B. Lund, O. P. Persson, C. O. Collins, et al. (2017), Calibrating a viscoelastic sea ice model for wave propagation in the arctic fall marginal ice zone, *Journal of Geophysical Research: Oceans*.

Collins III, C. O., and W. E. Rogers (2017), A source term for wave attenuation by sea ice in wavewatch iii: Ic4, *Tech. rep.*, Naval Research Laboratory Stennis Space Center United States.

Collins III, C. O., B. Lund, R. J. Ramos, W. M. Drennan, and H. C. Graber (2014), Wave measurement intercomparison and platform evaluation during the itop (2010) experiment, *Journal of Atmospheric and Oceanic Technology*, *31*(10), 2309–2329.

Collins III, C. O., W. E. Rogers, A. Marchenko, and A. V. Babanin (2015), In situ measurements of an energetic wave event in the arctic marginal ice zone, *Geophysical Research Letters*, *42*(6), 1863–1870.

Collins III, C. O., W. E. Rogers, and B. Lund (2017a), An investigation into the dispersion of ocean surface waves in sea ice, *Ocean Dynamics*, *67*(2), 263–280.

Collins III, C. O., B. Blomquist, O. Persson, B. Lund, W. Rogers, J. Thomson, D. Wang, M. Smith, M. Doble, P. Wadhams, et al. (2017b), Doppler correction of wave frequency spectra measured by underway vessels, *Journal of Atmospheric and Oceanic Technology*, *34*(2), 429–436.

Doble, M. J., J. P. Wilkinson, L. Valcic, J. Robst, A. Tait, M. Preston, J.-R. Bidlot, B. Hwang, T. Maksym, and P. Wadhams (2017), Robust wavebuoys for the marginal ice zone: Experiences from a large persistent array in the beaufort sea, *Elem Sci Anth*, *5*.

Donelan, M. A., J. Hamilton, and W. Hui (1985), Directional spectra of wind-generated waves, *Philosophical Transactions of the Royal Society of London A: Mathematical, Physical and Engineering Sciences*, *315*(1534), 509–562.

Fox, C., and T. G. Haskell (2001), Ocean wave speed in the antarctic marginal ice zone, *Annals of Glaciology*, *33*(1), 350–354.

Hauser, D., K. Kahma, H. E. Krogstad, et al. (2005), Measuring and analysing the directional spectra of ocean waves.

Herbers, T., S. Elgar, N. Sarap, and R. Guza (2002), Nonlinear dispersion of surface gravity waves in shallow water, *Journal of physical oceanography*, *32*(4), 1181–1193.

Kinsman, B. (1965), *Wind waves: their generation and propagation on the ocean surface*, Courier Corporation.

Krogstad, H. E. (2002), Second order wave spectra and heave/slope wave measurements, in *Ocean Wave Measurement and Analysis (2001)*, pp. 288–296.

Krogstad, H. E., and K. Trulsen (2010), Interpretations and observations of ocean wave spectra, *Ocean Dynamics*, *60*(4), 973–991.

Lamb, H. (1932), *Hydrodynamics*, Cambridge university press.

Leckler, F., F. Ardhuin, C. Peureux, A. Benetazzo, F. Bergamasco, and V. Dulov (2015), Analysis and interpretation of frequency–wavenumber spectra of young wind waves, *Journal of Physical Oceanography*, *45*(10), 2484–2496.

Longuet-Higgins, M. S. (1963), Observations of the directional spectrum of sea waves using the motions of a floating buoy, *Ocean wave spectra*, pp. 111–136.

Lund, B., H. C. Graber, H. Tamura, C. O. Collins III, and S. M. Varlamov (2015), A new technique for the retrieval of near-surface vertical current shear from marine X-band radar images, *J. Geophys. Res. C: Oceans*, *120*(12), 8466–8486, doi:10.1002/2015JC010961.

Marchenko, A., A. Shestov, E. Karulin, E. Morozov, M. Karulina, P. Bogorodsky, S. Muzylev, D. Onishchenko, and A. Makshtas (2011), Field studies of sea water and ice properties in svalbard fjords, in *Proceedings of the International Conference on Port and Ocean Engineering Under Arctic Conditions*, POAC11-148.

Marko, J. R. (2003), Observations and analyses of an intense waves-in-ice event in the sea of okhotsk, *Journal of Geophysical Research: Oceans*, *108*(C9).

Marsan, D., J. Weiss, E. Larose, and J.-P. Métaxian (2012), Sea-ice thickness measurement based on the dispersion of ice swell, *The Journal of the Acoustical Society of America*, *131*(1), 80–91.

Newyear, K., and S. Martin (1999), Comparison of laboratory data with a viscous two-layer model of wave propagation in grease ice, *Journal of Geophysical Research: Oceans*, *104*(C4), 7837–7840.

Rogers, W. E., and S. Zieger (2014), New wave-ice interaction physics in wavewatch iii, *Tech. rep.*, NAVAL RESEARCH LAB STENNIS DETACHMENT STENNIS SPACE CENTER MS OCEANOGRAPHY DIV.

Rogers, W. E., J. Thomson, H. H. Shen, M. J. Doble, P. Wadhams, and S. Cheng (2016), Dissipation of wind waves by pancake and frazil ice in the autumn beaufort sea, *Journal of Geophysical Research: Oceans*, *121*(11), 7991–8007.

Squire, V. A. (1993), A comparison of the mass-loading and elastic plate models of an ice field, *Cold regions science and technology*, *21*(3), 219–229.

Squire, V. A., and A. Allan (1977), *Propagation of flexural gravity waves in sea ice*, Centre for Cold Ocean Resources Engineering, Memorial University of Newfoundland.

Stokes, G. G. (1847), On the theory of oscillatory waves, *Trans Cambridge Philos Soc*, *8*, 441–473.

Sutherland, G., and J. Rabault (2016), Observations of wave dispersion and attenuation in landfast ice, *Journal of Geophysical Research: Oceans*, *121*(3), 1984–1997.

The WAVEWATCH III ® Development Group (2016), User manual and system documentation of WAVEWATCH III ® version 5.16, *Tech. Note 329*, NOAA/NWS/NCEP/MMAB, 326 pp. + Appendices.

Thomson, J., and W. E. Rogers (2014), Swell and sea in the emerging arctic ocean, *Geophysical Research Letters*, *41*(9), 3136–3140.

Thomson, J., J. Talbert, A. de Klerk, A. Brown, M. Schwendeman, J. Goldsmith, J. Thomas, C. Olfe, G. Cameron, and C. Meinig (2015), Biofouling effects on the response of a wave measurement buoy in deep water, *Journal of Atmospheric and Oceanic Technology*, *32*(6), 1281–1286.

Thomson, J., S. Ackley, H. H. Shen, and W. E. Rogers (2017), The balance of ice, waves, and winds in the arctic autumn, *Eos*, *98*.

Toba, Y. (1973), Local balance in the air-sea boundary processes, *Journal of Oceanography*, *29*(5), 209–220.

Tucker, M. (1989), Interpreting directional data from large pitch-roll-heave buoys, *Ocean Engineering*, *16*(2), 173–192.

Tucker, M. J., and E. G. Pitt (2001), *Waves in ocean engineering*, Volume 5.

Wadhams, P., and B. Holt (1991), Waves in frazil and pancake ice and their detection in seasat synthetic aperture radar imagery, *Journal of Geophysical Research: Oceans*, *96*(C5), 8835–8852.

Wadhams, P., and J. Thomson (2015), The arctic ocean cruise of r/v sikuliaq 2015, an investigation of waves and the advancing ice edge, *Il Polo*, *70*(4), 9–38.

Wadhams, P., V. A. Squire, D. J. Goodman, A. M. Cowan, and S. C. Moore (1988), The attenuation rates of ocean waves in the marginal ice zone, *Journal of Geophysical Research: Oceans*, *93*(C6), 6799–6818.

Weitz, M., and J. B. Keller (1950), Reflection of water waves from floating ice in water of finite depth, *Communications on Pure and Applied Mathematics*, *3*(3), 305–318.

Young, I. (1994), On the measurement of directional wave spectra, *Applied Ocean Research*, *16*(5), 283–294.